Materials Science in Semiconductor Processing 121 (2021) 105367

Contents lists available at ScienceDirect

Materials Science in Semiconductor Processing

journal homepage: http://www.elsevier.com/locate/mssp

Correlation and optimization of the optoelectrical properties of DC magnetron-sputtered Cu_2ZnSnS_4 absorber layer as a function of the material composition

Maria Zhukova [a,*], Ratan Kotipalli [b], Olivier Poncelet [c], Louise Samain [b], Lionel Fourdrinier [b], Denis Flandre [a]

[a] ICTEAM, UC Louvain, Place du Levant 3, 1348, Louvain-la-Neuve, Belgium
[b] CRM Group, Allée de l'Innovation 1, B57- Quartier Polytech 3, 4000, Liège, Belgium
[c] IMAP, UC Louvain, Place Sainte Barbe 2, 1348, Louvain-la-Neuve, Belgium

ARTICLE INFO

Keywords:
CZTS
Sputtering
Rapid thermal processing
Optoelectrical properties
Simulation

ABSTRACT

Sequential DC magnetron sputtering and rapid thermal processing appear very promising to fabricate CZTS-based thin-film photovoltaic (PV) solar cells with regards to existent environmental and industrial issues. However, their state-of-the-art efficiency remains limited to about 10% to date. In this work, we aim at optimizing the optical and electrical properties of the CZTS absorber by an extensive screening of their correlation with the material composition. This is widely varied by different deposition (i.e. thickness of precursors) and process (i.e. RTP) conditions. We assess the impact of absorber composition on the energy bandgap, absorption coefficient, p-type carrier concentration and mobility. The most important results lie in the extensive analysis of the inverse power-law trend for carrier concentration versus mobility and logarithmic trend versus bandgap. Our conclusions point the optimal composition ratios towards Cu-poor and less than actual target Zn-rich range. As a result, a potential roadmap is drawn up based on presented experimental results and SCAPS simulations in order to reach more than 10% cell efficiency with the target technology.

1. Introduction

The pure sulphide kesterite compound - Cu_2ZnSnS_4 (CZTS) is considered as a promising absorber for photovoltaic (PV) solar cell application thanks to its suitable band gap (E_g ~1.5 eV) and high absorption coefficient ($\alpha \sim 10^4\ cm^{-1}$) [1,2]. Moreover, for environmental and industrial considerations, all elements are earth-abundant and non-toxic when compared to other chalcopyrite CIGS and kesterite CZTSe semiconductors. In terms of industrial fabrication, magnetron sputtering of precursor followed by sulfurization via rapid thermal annealing process (RTP) positions as a highly suitable two-step method [3].

Unfortunately, the synthesis of the phase of this quaternary semiconductor compound optimal for PV application appears difficult to control [4], notably due to the uneasy reproducibility of thermal treatment, which brings about many of the limiting factors in CZTS-based PV cells. Among them, the significant interface and bulk recombination [5], high series (R_s), low shunt (R_{sh}) resistances [6] and barrier formation at back contact interface [7,8] have been mentioned in relation to the CZTS material properties.

Ab initio calculations predict low formation energy of shallow (*CBM/VBM* ± 0.2 eV) acceptor defects like Cu_{Zn} +0.12 eV, V_{Cu} +0.02 eV, which results in doping density and p-type conductivity. At the same time, they cause structural disorder in CZTS [9].

Many studies have been carried out to make progress in CZTS thin layers synthesis and characterization. Most of them indicate that a copper-poor, zinc-rich region is suitable for photovoltaic application [3,10,11] and typically aims for the kesterite thin films to be in the compositional ratio ranges of 0.76–0.90 for Cu/(Zn + Sn) and 1.1–1.3 for Zn/Sn ratios. Only few experimental in-depth electrical investigations link material composition and optoelectrical [12,13] or transport properties [14,15]. Most of the studies are focused on the impact of the material properties or device processing conditions on the final PV cell device performances. This approach does not allow to fully understand the complex optimization of the absorber optoelectronic parameters in order to break the *10%* efficiency limit of pure CZTS-sputtered cells [11,16,17].

* Corresponding author. Tel.: +3210472609; fax: +3210478705.
E-mail address: maria.zhukova@uclouvain.be (M. Zhukova).

https://doi.org/10.1016/j.mssp.2020.105367
Received 30 October 2019; Received in revised form 28 March 2020; Accepted 1 August 2020
Available online 20 September 2020

In a previous work [18], the optoelectronic parameters were linked to cell performances through simulations with 1-D Solar Cell CaPacitance Simulator [19,20] (SCAPS, University of Ghent, Belgium). Using the measured CZTS optoelectronic properties as starting inputs to the SCAPS simulator, the impacts of each key optoelectronic parameter on cell performance were clearly distinguished. In order to reach *10%* cell efficiency, the targeted CZTS properties were established as: $Eg \sim 1.6$ eV; average absorption in *300* – 1000 nm wavelength range $\alpha_{avg} \sim 3.5 \times 10^4\ cm^{-1}$; majority carrier concentration $p \sim 5.5 \times 10^{15}\ cm^{-3}$ and hole mobility $\mu_h \sim 25\ cm^2\ V^{-1}\ s^{-1}$ [18]. As a result, those simulations showed that the sputtered CZTS layers could achieve the *10%* efficiency limit after full sequential optimization of all layers.

The present paper aim is firstly to further corroborate the variation of the optoelectrical properties of CZTS layers, in a very large (but controlled) range, as a function of the material composition, secondly to establish the mobility versus carrier concentration inverse power-law trend for CZTS, thirdly to re-examine the best recommended atomic % ratios of the elements towards highest cell efficiency. To our best knowledge, such results have not been discussed before. In this study we obtain different sample groups with widely different compositions using different precursor thicknesses, sulfurized by similar or slightly different RTP conditions, in the same environment. The optoelectrical measurements of the different sample groups are next compared and correlated with their material compositions. The aim of this systematic study is to understand the optoelectrical properties trends with composition ratios for different precursor thicknesses and Rapid Thermal Processing (RTP) conditions. To allow that study, we have to focus here on the CZTS films deposited and grown on glass substrate only, without considering the Mo back contact and other subsequent layers or interface effects.

In Section 2, fabrication details about precursor deposition and sulfurization conditions are presented together with measurement techniques for material, optical and electrical characterizations of thin layers. In Section 3, results and discussions are presented for all fabricated samples and compared with reference [18] and new target points for high-efficiency cells. They are corroborated by correlations of optoelectrical and material compositions. Finally, conclusions and future perspectives are drawn up in Section 4.

2. Material and methods

2.1. Precursor deposition and sulfurization step

a. Precursor deposition: Different research groups reported that the quality of CZTS films and/or CZTS-based device performances is influenced by the sequences in the stacking of layers [21–30]. This work presents results only for the glass/**Cu/Sn/Zn** stack order, which showed the best adhesion to the glass substrate and the best homogeneity after the sulfurization [18]. Results can be different on Mo but without strongly affecting the relative trends concerning the final resulting material compositions, mostly correlated with the amounts of deposited CZT precursors and of S in the RTP chamber. Furthermore, passivation layers are more and more used in thin-film PV cells at the absorber/Mo interface to reduce carrier recombination at the back contact. Such passivation layers are based on insulating oxides, Al_2O_3 having been identified as the most efficient for p-type absorbers [31] with properties closer to a glass than to a metal [32].

Each precursor layer was processed by direct current (DC) magnetron sputtering onto 2 mm-thick soda lime glass. The coating step was carried out at room temperature from pure (99.99%) 76.2 mm-diameter targets. The substrates were placed at a distance of 110 mm from targets and put in rotation at 10 rpm during the deposition step. The base pressure in the sputtering chamber was about 10^{-6} Torr, the work pressure was about 2.4 mTorr with a fixed Ar flux of 30 sccm. More details about process conditions can be found in Ref. [18].

Three different groups - *Small (S)*, *Medium (M)* and *Large (L)* - of metallic precursor with a total increasing stack thickness of ~300 nm, ~500 nm, ~600 nm respectively, but constant composition ratios were processed. The literature **reference compositional ratios** of Cu/(Zn + Sn) ~ 0.76 and Zn/Sn ~ 1.22 and corresponding atomic percentages were fixed for the copper-poor, zinc-rich [3,27,33] deviation from the stoichiometry with **Cu~21.5%, Zn~15.6%, Sn~12.8%, S~50%** atomic weights, this deviation being considered to be the most efficient for PV cell application in Ref. [11,34]. Published efficiency mappings [33] for CZTS solar cells confirm the suitability of the chosen ratios.

b. Sulfurization step: The two most used ways for introducing sulphur into a metallic precursor are either to use a sulphur compound gas like H_2S [33] or to place elemental sulphur into the reactive chamber together with precursor during the thermal treatment [26]. The advantage of the latter is its lower toxicity risk and easier applicability. In addition, fast heating for RTP process is considered the most suitable way to avoid secondary phases formation [35]. Several studies have been published on the effect of the annealing condition (pressure [36], time [37], temperature [38]…). In this study, the precursor thickness was varied with limited modifications of sulfurization conditions. Our precursors were finalized into CZTS thin layers by RTP in an AS-ONE 100 furnace under Ar atmosphere with a presence of solid sulphur and at a pressure of 0.9 bar before heating up. Four different RTP configurations were applied on the same precursors from the 3 groups (Table 1). During all RTP runs, sample was installed inside the susceptor cavity together with additional compounds (i.e. sulphur (S), tin sulphide (SnS), or tin (Sn)). The same graphite susceptor with graphite lid was used for all runs, placed into the furnace chamber and heated up from the top by infrared radiation of reactor's lamps. The thermal profile includes a ramp till 550 °C at a rate of 3 °C/s, followed by a curing at fixed (550 °C) temperature during 5 min in the same chamber. This is a relatively short time for RTP processing which are usually reported to range from 3 [35] to 15 [25] minutes. This duration was fixed for all precursor thicknesses and should further be studied but is not the scope of current paper that focuses on varying the final material composition. At the end, the samples were cooled down to room temperature inside the reactor with an estimated cooling rate of about ~24 °C/min.

During *standard RTP 1*, the samples were placed inside the graphite susceptor together with solid sulphur pellets at the four corners of the susceptor with total mass *m(S)* ~100 mg and additional *4 × SnS* pellets

Table 1
Process details for three sample groups (sample size *~40 × 40 mm²*, except for *RTP 1* series that used *~20 × 20 mm²*) and sample denominations.

Deposition Cu/Sn/Zn stack:	Small	Medium	Large
Material densities per unit area, g/m²:	0.8/0.88/0.6	1.33/1.48/1.00	1.67/1.86/1.25
Sputtering times, s:	380/677/193	633/1138/322	795/1430/403
Equivalent thicknesses, nm:	89/117/83	149/197/138	187/248/173
RTP configurations/RTP conditions:		@ Ar, 0.9 bar, 3 °C/s up to 550 °C during 5 min	
RTP 1: m(S)~100 mg; 4×SnS	**S1**	**M1**	**L1**
RTP 2: m(S)~100 mg; 4×SnS; m(Sn)~10 mg	**S2**	**M2**	**L2**
RTP 3: m(S)~100 mg; 4×SnS	**S3**	**M3**	**L3**
RTP 4: m(S)~40 mg; 4×SnS; m(Sn)~10 mg	**S4**	**M4**	**L4**

of total mass *m(SnS)* ~30 mg. The four pellets of *SnS* had been used before and were the same during all RTP runs in this study. They did not vary in volume, colour or shape.

For *RTP 2*: additional tin powder *m(Sn)* ~10 mg was placed inside the box to ensure its high partial pressure and avoid tin evaporation from precursor. Moreover, the sulphur pellets were placed at the corners of the glass substrate, to make them closer to the metallic stack and to avoid an eventual reaction with carbon/graphite susceptor [39].

For *RTP 3*, the sulphur pellets were placed at 8 different positions at the sample perimeter (4 corners and 4 semi-lengths of sample sides). The pellets were smaller in diameter, to ensure constant total mass. *SnS* was kept, but no additional tin powder was used.

During those *RTP 1, RTP 2 and RTP 3*, the graphite box was covered with a graphite lid to ensure semi-closed condition, and a quartz bell was placed over graphite box to homogenize the heating flux.

During the last *RTP 4*, half of the initial solid sulphur *m(S) ~40 mg* with smaller pellet size and tin powder mass *m(Sn) ~10 mg* was used in addition to *SnS*. The lid was kept elevated to ensure semi-opened condition, without the quartz bell.

In the last two *RTP 3* and *RTP 4*, the inner side of the chamber was cleaned to avoid a residual deposition from the previous runs and ensure the stability of the sulphur partial vapour pressure.

2.2. CZTS film characterization

In total, 12 different sample types were fabricated. They are listed in Table 1 where the letters *S*, *M* and *L* indicate the small, medium and large deposited precursor thicknesses and numbers *1* to *4* indicate *RTP* conditions. For all samples, material and optoelectrical characterizations were performed.

Composition and morphology of the thin films were analysed using a Field Emission Gun Electron Microscope (FEG-SEM, ULTRA55) with integrated Energy Dispersive X-Ray (EDX) spectroscopy analyses. The overall composition was estimated as the average of nine spectra scans, each at different points (with spot area 5 × 5 μm^2) over a 2 × 2 mm^2 area.

Raman spectroscopy measurements were performed for crystal structure analyses, with a LabRAM HR 800 instrument from Horiba Scientific. A green laser (514 nm) and a 2400 grooves/mm grating were used. The laser was focused onto the sample using a 100x objective with N.A. = 0.95 (spot size ~1 μm) and repeated at least at 3 different points on 5 × 5 mm^2 sample.

The **optical properties** of CZTS layers were analysed with a Perkin-Elmer LAMBDA 950 spectrometer equipped with a 150 mm integrating sphere. The hemispherical transmittance and reflectance spectra were recorded in the 250–2500 nm wavelength range over the central region of the samples through an entrance aperture window of 32 mm in diameter. This configuration allows accurate absorbance (A = 100 – R – T) calculations. The absorption coefficient is calculated using the following equation [40]:

$$\alpha = \frac{1}{d} ln\left(\frac{1-R}{T}\right) \quad \text{(Eq.1)}$$

where *d* is the thickness of the measured thin film. Finally, the bandgap values were estimated from a linear fit in the Tauc's plot. In addition, the Urbach energy is extracted from the slope of the linear fit of $ln(\alpha)$ vs. energy plot.

Electrical properties were obtained via Hall measurements using the Van der Pauw configuration using a commercial Ecopia HMS-3000 system [41] with a permanent magnetic field of 0.55 T. Hall measurements were performed on the final glass/CZTS layer samples obtained after sulfurization step. A square piece of 5 × 5 mm^2 was cut from each studied sample and indium drops were soldered at each corner. The golden-coated tips of spring clip board were used to improve the electrical contact with indium. Each measurement is performed twice, at constant amplitudes, but with opposite signs of magnetic field (as a limit of single oscillation approximation of AC magnetic field in Gunawan et al. [42]). We used a delay time between each measurement point up to several tens of seconds, which corresponds to the attenuated oscillation time in a parallel dipole line system [42] and satisfies the equilibrium condition. The delay has to be increased for higher doping, which can be reasonable to achieve the equilibrium condition.

Measurement were conducted at controlled room temperature of 21 ± 0.5 °C. A sample measurement case filled with nitrogen gas was used to decrease the surface (film/air) interaction and recombination in thin film, that measure should play beneficial role for noise and background conditions.

Thanks to this robust procedure, reproducible measurements have been obtained for each sample. Each sample was measured 20 times. The average values and standard deviations of carrier concentration - *p* and hole mobility - μ_h can then be fairly compared.

3. Results and discussion

3.1. Material characterizations

a. EDX results: the different RTP conditions/configurations impact the partial pressures of S and Sn in the chamber. Since both are difficult to control inside the processing chamber during RTP, **the following discussion is based on the final overall composition of CZTS layers.** The average atomic percentages calculated for all characterized CZTS layers are reported in Table 2, the standard deviation being less than 1%.

Even with dispersion of results within each group, it is evident that all samples of the *S* group were highly Cu-poor and Zn-rich compared to the stoichiometry and literature-reference ratios. The samples from the *L* and *M* groups contained more copper (except of M3) and showed opposite tendency for the Cu/(Zn + Sn) and Zn/Sn ratios. Additional tin powder during *RTP 2* increases the Zn/Sn ratio and thus getting close to the reference - 1.22 ratio for Medium and Large samples. *RTP 3* tends to incorporate more sulphur in thinner films (S3 and M3). The samples after *RTP 4* with low initial sulphur all show the minimal deviation from the target value of 50 % which could be considered as suitable condition to get this value.

b. SEM results: Fig. 1 presents the SEM results of in-plane views. From cross-section views (see Appendix 1), the CZTS thicknesses were estimated to be about ~1 μm, ~1.5 μm and ~2 μm respectively for *S, M, L* groups. In both in-plane and cross-section views, the estimated grain sizes are equal to 100 nm, 100–800 nm, 50–600 nm in *S, M, L* samples respectively.

The samples in the *S* group show compact, dense morphology without delamination problems at the interface with glass. On the other hand, voids were formed at the glass/CZTS interface for samples in *M* and *L* groups. Similar voids formation [43] was previously observed by other research groups and has been explained by the CuS_2 secondary phase formation [12] or by heating rate effect [11] or by liquid phase Sn [44]. In this study the voids formation has been related to sulphur concentration, the more sulphur the more bubbles, so that voids were observed when increasing the level of sulphur. We do not expect the adhesion problems to have a very significant impact in the next opto-electronic results since these are localized and measurements are repeated at several positions of the samples.

c. Raman results: Fig. 2 shows Raman results measured on all CZTS thin layers. The results confirm the presence of the main peaks (black arrows in Fig. 2) from CZTS around 286, 336 and 368 cm^{-1} in each sample [45]. The main peak exact positions only slightly vary from about 333 cm^{-1} for *L2*, to 335 cm^{-1} for *S1, M1, L1, M3, L4* and 336 cm^{-1} for *M2, M3, L3*.

Very weak peaks from secondary phases can be slightly distinguished at low ~180 cm^{-1} from Sn_2S_3 and at ~680 cm^{-1} from ZnS. Moreover, the additional peak intensities at 286 cm^{-1} and 368 cm^{-1} are also weak and were explained by the cations disorder in the structure [46,47].

Table 2
Overall average composition (in at.%) of each type of samples compared to stoichiometric (Stoi) and PV-optimal literature reference (Ref) values [27].

at.%	Stoi	Ref	S1	S2	S3	S4	M1	M2	M3	M4	L1	L2	L3	L4
Cu	25	21.5	18.5	18.8	17.3	19.6	24.0	21.2	18.5	23.4	23.2	23.4	22.9	22.8
Zn	12.5	15.6	16.5	17.4	17.4	19.3	11.1	12.1	8.7	12.5	7.3	9.7	12.5	12.1
Sn	12.5	12.8	12.3	11.5	11.8	11.5	14.9	14.5	16.8	13.5	15.9	14.6	13.6	14.5
S	50	50	52.7	52.2	53.5	49.6	50.0	52.2	56.0	50.6	53.6	52.3	51.0	50.7

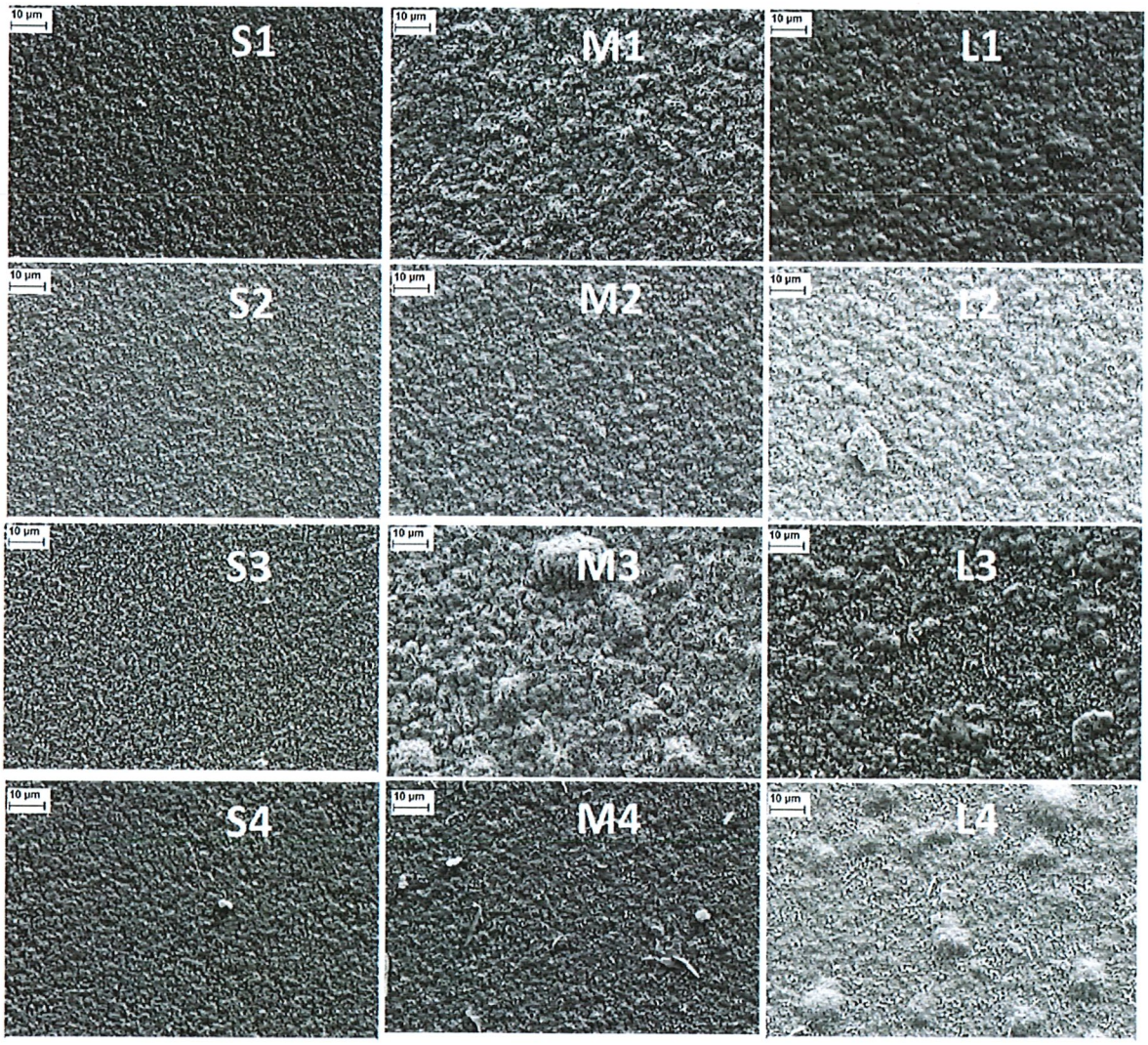

Fig. 1. In-plane views for all samples. The bar scale in the upper left corner of each view corresponds to 10 µm.

Finally, rather small signs of presence of secondary phases appear at low 100–250 cm^{-1} for Sn_2S_3 and at high ~680 cm^{-1} for ZnS, while no sign of Cu_2S could be observed. As a result, all the next optoelectronic results can be fairly related to CZTS.

3.2. Optoelectrical characterization

a. UV–vis results discussion: The measured transmission (*T(λ),%*) and reflection (*R(λ),%*) spectra allow accurate absorption calculations as mentioned above (Eq. (1)). The absorption spectra results depend on the characterization technique and method of calculation [4,40,48]. The absolute values of bandgaps and Urbach energies depend as well on the range of linear extrapolation. For this study the method described in Hassanien et al. [48] is applied for transmission T(λ) and reflection R(λ) data measured with spectroscopy technique. For extrapolations the most linear range was considered after the absorption edge (Appendix 2).

Fig. 3 shows the absorption coefficient spectra obtained for each RTP and S-M-L sample types. The spectra show that as expected, the absorption coefficient increases within whole spectrum by increasing the CZTS thickness, except the samples L1 below 620 nm. In this wavelength range, the spectra of M, L groups after *RTP 2*, *RTP 3* and *RTP 4* presents signs of some interference. This can be explained by the layer roughness as observed in SEM views and its impact on the reflection spectra.

From analysis of average values, the lowest average absorption coefficient in visible spectrum is for *L1* and is equal to 2.9×10^4 cm^{-1}. The highest average value is equal to 6.5×10^4 cm^{-1} for *L3* sample.

Comparing by group, all samples in *S group* show similar results except the sample after last *RTP 4* run – the lowest one within this group. The results for *M* group showed higher absorption coefficients after *RTP 4* and *RTP 3*, but lower after *RTP 2* and *RTP 1*. Within both groups *M* and *L*, the average absorption coefficient increases from RTP conditions 1 to 3. The highest average values for *M3* and *L3* samples are equal to 5.8×10^4 and

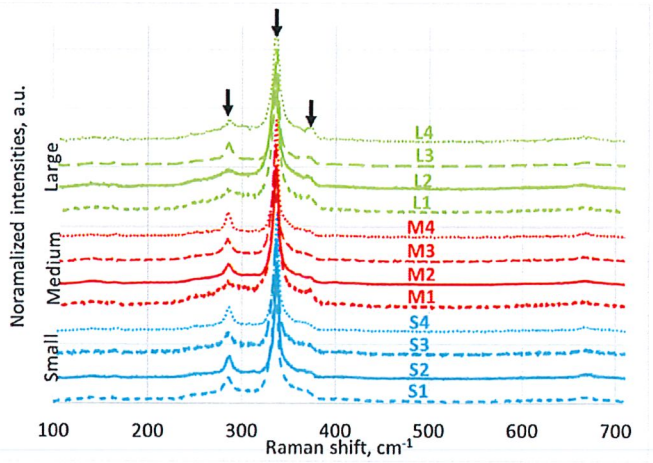

Fig. 2. The Raman spectra performed on all the processed samples. Arrows indicate the main peaks position.

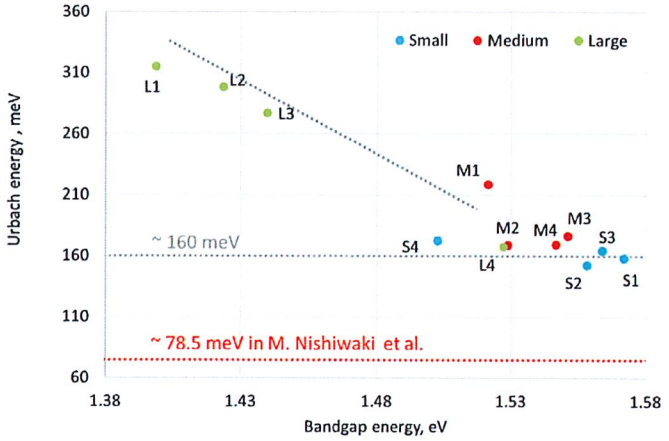

Fig. 4. Extracted Urbach energy versus corresponding bandgap energy for all samples together with experimental data [49] (in red), tendency and saturated limit (in grey).

6.5×10^4 cm^{-1} respectively. Moreover, the samples after *RTP 4* showed the highest average absorption coefficient within Medium and Large groups, which could indicate more favourable processing conditions and probably links to the low/smaller grains used for ambient sulphur concentration. Overall, all values appear convenient for our next SCAPS target. In a conservative approach, an average absorption coefficient of 4×10^4 cm^{-1} will be considered in the simulations to focus on other trends.

The results of extracted bandgaps and Urbach energies from the corresponding linear fits are presented together for all sample types in Fig. 4.

The results show the different bandgaps measured for S, M, L groups and the limited dispersion within each group after *RTP 1*, *RTP 2* and *RTP 3*. The variations can be explained by the fixed curing time used for different thicknesses of precursors and the bandgap compositional dependence as discussed in Malerba et al. [12]. The results after *RTP 4* bring all three groups together with smaller dispersion and indicate that the amount of present sulphur varies the bandgap, independently of thickness. Bandgaps decrease from *S* to *L* from *1*.58eV to *1*.37eV. This tendency is less pronounced for samples after *RTP 4*, where bandgap varies from 1.50 to 1.53eV from S to L. The S2 sample in the *S* group shows the highest bandgap for the CZTS compound and could be interesting to consider in the cases of ultrathin [8] or tandem structures [50]. The samples of *M* and *L* groups are suitable for single junction solar cell application due to their near optimal bandgap range.

The group of the *S* - samples have an abrupt transition from absorption to transmission zones, which results in the low Urbach tails, saturating at

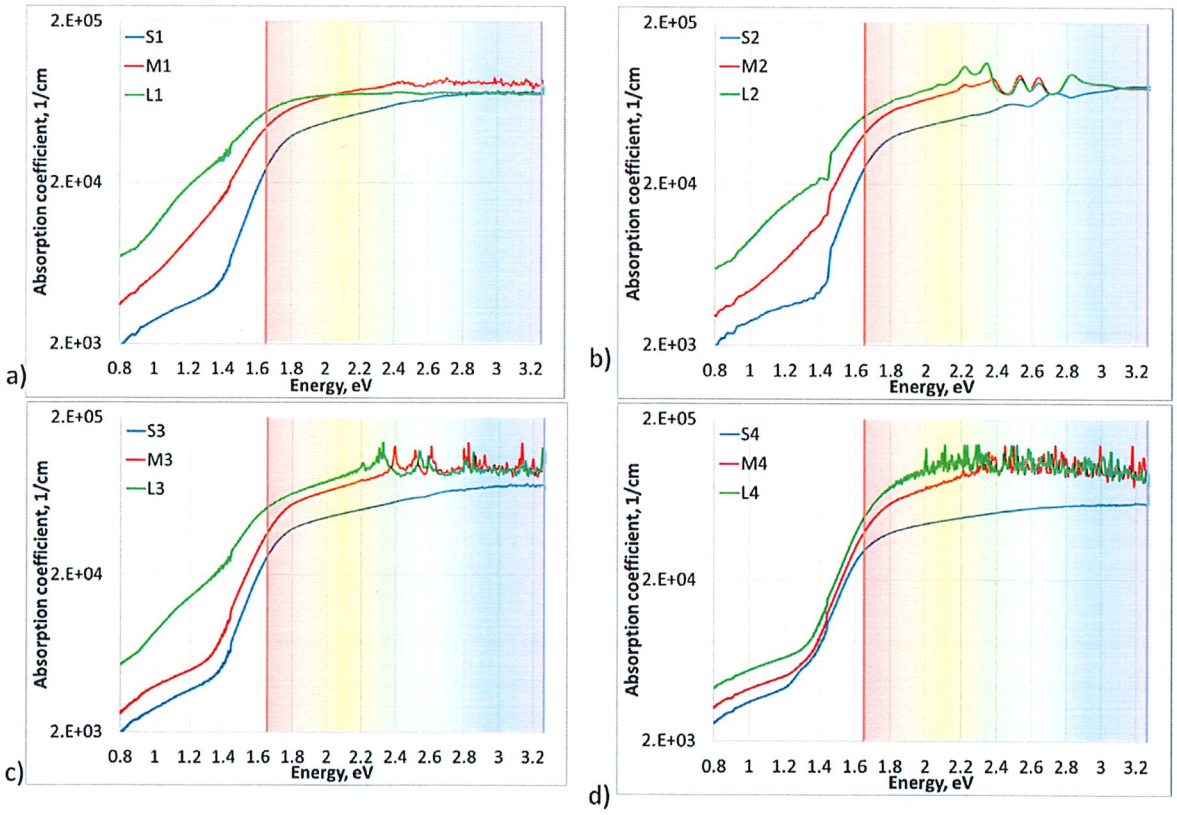

Fig. 3. The absorption coefficient spectra as a function of energy for a) *RTP 1*; b) *RTP 2*; c) *RTP 3* and d) *RTP 4* together with visible range in rainbow colours.

~160 meV. The Urbach energies increase from about 150 meV in group *S* to 320 meV in group *L* for all samples of *RTP 1–3*, while all *RTP 4* samples show tails values between 170 meV and 190 meV. Samples from *RTP 4* show the most abrupt transitions, almost regardless of the precursor thickness. This could link to the sulphur quantity present in the reaction chamber, being an indication for suitable processing conditions. The saturation minimum at ~160 meV for all experimental results is twice higher compared to Nishiwaki et al. [49] or Malerba et al. [40] and 5 times higher than the theoretical limit of 30 meV for single crystal CZTS [49] and experimental results discussed in Rey et al. [4]. For improving that, additional post-process annealing in e.g. hydrogen atmosphere can be proposed.

The effect of bandgap fluctuation on the band tailing was previously discussed and linked to the voltage deficit of PV cells by interface recombination [51]. In the same paper, Gokmen et al. explained the band-tailing by electrostatic potential fluctuation in terms of bulk defects. In this study, the effect and correlation of optoelectrical parameters with material composition are discussed below in section 3.3.

b. Hall measurement results: It is not easy to systematically ensure the required processing conditions for forming only favourable point defects (V_{Cu}^{-}, Cu_{Zn}^{-}) for CZTS p-type conductivity. If we assume that each formed electrically-active defect will give rise to one free carrier, then the measured carrier concentration can be directly linked to defect concentration.

Fig. 5 presents the results of electrical characterization in a log-log graph showing mobility versus carrier concentration. They can be related by a fit of $\mu_h = 4 \times 10^6 \times p^{-0.4}$ *power-law* function, where all experimental points of this study are enclosed in region limited by top and bottom dotted lines, which correspond maximum (3×10^7) and minimum (2×10^6) values for the fitting coefficient. This empirical fitting confirms thermionic conduction mechanism via ionized defects [14]. Results show a large range of electrical properties from low (10^{11} cm^{-3}) to high (10^{19} cm^{-3}) carrier concentrations, while the mobility varies from *100* to *0.07* $cm^2V^{-1}s^{-1}$ respectively. The inverse proportionality trend for mobility versus carrier concentration validates that the main recombination effect on mobility is due to ionized defects affecting carrier concentration.

The precursor thickness impacts the final carrier concentration for similar *RTP 1* and *RTP 2* conditions, resulting into higher p and lower μ_h, than in other samples of the same group. At the same time, the introduced sulphur mass and/or *RTP* configuration dramatically change the results after *RTP 4*, shifting them to a low p with high μ_h range.

The results in Fig. 5 clearly indicate the absence of the experimental point at middle-doped range ~$10^{14\text{-}15}$$cm^{-3}$, which probably relates to the small stoichiometrical window in CZTS phase diagram. The experimental samples *M2* and *L3* approach better the target carrier concentration region but still need mobility improvement. For this, further RTP conditions can be studied: sulphur grain size, heating ramp etc., an additional post-annealing step can also be proposed. Finally, the experimental points from other research groups either exhibit the same problem of low mobility in the heavy-doped region.

The results after *RTP 3* are closer to the target SCAPS values for *M3* and *L3* samples as discussed below. The introduced sulphur pellet diameter thus appears essential for the partial pressure control and its homogenous distribution over the precursor should be assured.

3.3. Optoelectrical and material results correlations

To re-establish ***our target*** for optimal optoelectronic properties of the absorber, we performed SCAPS simulation for intrinsic cell, i.e. with fixed resistances $R_s = 0$, $R_{sh} = infinite$ and flat band conditions at back ohmic contact. The thickness (*th*) and average absorption coefficient over visible range were kept fixed and chosen as middle values in studied series and literature: $th = 1.5$ µm and $\alpha_{avg} = 4 \times 10^4\ cm^{-1}$. This simplification was done to restrict the simulation results and focus the discussion on the parameters that vary by orders of magnitude, i.e. carrier concentration and mobility, but it is evident that efficiency will increase with increase of α_{avg}. The independently varied parameters were then E_g, p and μ_h (using a typical $\mu_e = 4 \times \mu_h$ ratio for electron mobility), then mobility and concentration were varied based on the $\mu_h \sim p^{-0.4}$ trend established from Hall measurements. Despite that our results correspond to in-plane or lateral mobility, we expect the vertical mobility, of importance in real cell operation and SCAPS simulation, to be correlated. Given the ion-transport mechanisms assumed by the inverse $p\ x\ \mu_h$ power law and the similar grain sizes observed in in-plane and cross-section SEM views, we consider the Hall experimental results as fair starting points. More detailed information about other baseline parameters used in SCAPS simulation are presented in Ref. [18] and Appendix 3.

Fig. 6 show the simulation results of cell efficiency versus carrier concentration for different band gaps and mobility levels, compared with two experimental data from literature. The efficiency obtained for carrier concentration in the range of 10^{17}-10^{19} cm^{-3} for fixed mobilities is limited by a plateau, while an ***optimal range*** is reached at about

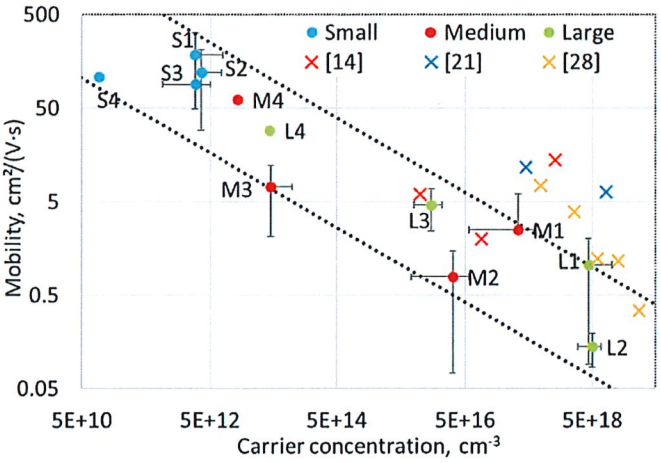

Fig. 5. Hall measurement values of mobility versus carrier concentration (average values are represented by dots for all our sample types and standard deviations by error bars (for selected samples), along with available literature data (crosses). The dotted lines represent the inverse power-law tendencies for minimum and maximal fitting coefficient.

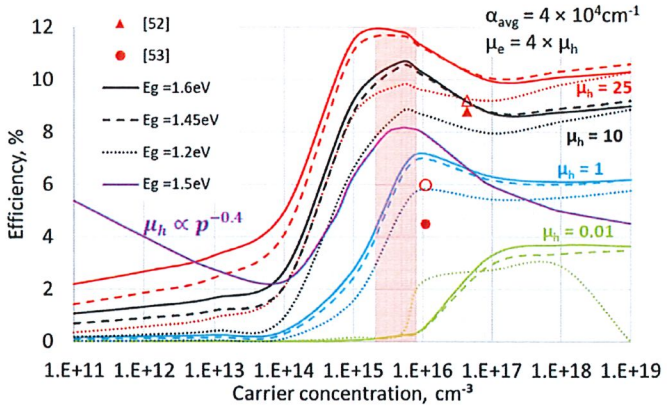

Fig. 6. SCAPS simulation results of intrinsic cell efficiency versus carrier concentration for different mobilities and bandgaps with optimal range (in pink) along with two experimental points (closed symbols) and their intrinsic efficiencies after removing shunt and series resistance effects (open symbols).

p ~2 × 10^{15}–8 × 10^{15} cm^{-3} with E_g ~1.4-1.6 eV and μ_h = 3–25 $cm^2V^{-1}s^{-1}$. This range covers the optimal set of values from previous calculation in Ref. [18] which was established as following: p ~5.5 × 10^{15} cm^{-3} with E_g ~1.6 eV and μ_h = 25 $cm^2V^{-1}s^{-1}$.

As shown in Fig. 6, the behaviour changes after 1.0 × $10^{17}cm^{-3}$, when doping density in absorber is higher than the doping of the buffer layer and leads to a lowering of cell performance. It is worth nothing that for highly doped cases ($p > 1 \times 10^{17}$ cm^{-3}) and relatively high mobilities (μ_h > 10 $cm^2V^{-1}s^{-1}$), the optimum moves towards lower bandgap values.

From studied CZTS layers, only *L3* is approaching the most favourable properties, but improving mobility is still required. This could be achieved for M and L groups by decreasing sulphur quantity in chamber, not as much as during *RTP 4*, as *M4*, *L4* samples significantly shifted to low-doping – high mobility range. An additional post processing treatment, like annealing, could be proposed for highly doped layers, while post-process doping could be tried for very low-doped layers.

The simulation results match well available experimental results after subtracting the resistances effect: R_s = 0.96 Ohm.cm^2, R_{sh} = 1492 Ohm.cm^2, p ~4.4 × 10^{16} cm^{-3}, E_g~1.54 eV and 8.8% cell efficiency [52] (9.2% without resistances) and R_s = 8 Ohm.cm^2, R_{sh} = 700 Ohm.cm^2, p ~1.1 × 10^{16} cm^{-3}, μ_h = 2.6 $cm^2V^{-1}s^{-1}$, E_g~1.51 eV and 4.5% cell efficiency [53] (6.0% without resistances). Mobility is hence the key parameter to improve.

Consequently, for this study, the ***optimal target range*** is fixed for ***values of*** E_g ~1.4-1.6 eV with carrier concentration about p ~ (2–8) × 10^{15} cm^{-3} and experimental achievable values for the correlation coefficient between p and mobility given by the $p \times \mu_h$ product ~ (0.6-20) × 10^{16} $cm^{-1}V^{-1}s^{-1}$.

This is a very important result since when achieving low mobility values, higher carrier concentration could appear favourable for a better efficiency as obtained in numerous articles. But this local optimum appears inadequate to break the 10% efficiency barrier. High mobilities are obviously needed but move the optimum carrier concentration to intermediate values. Our results also importantly show that can be made feasible in practice, following the inverse p x μ_h power law we have measured.

From results of Figs. 4 and 5, our samples show a pronounced correlation of bandgap decrease with carrier concentration increase. Fig. 7 presents the ***correlation coefficient*** $p \times \mu_h$ versus Cu/(Zn + Sn) ratio for all samples, compared with ***optimal target range***.

Samples M2 and L3 are found into the established optimal SCAPS range. The correlation between material and optoelectrical results put in evidence the tendency for carrier concentration to increase with Cu content (Fig. 7), which was already discussed in Ref. [18] and in literature [53].

All samples of the *S* – group showed Cu-poor composition with low p and high μ_h. Moreover, samples after *RTP4* aligned with the isoline for sulphur content *S ~50 at.%* and all others (except S3 and M3) with *S ~52 at.%*. The linear regression at S ~ 52 at.% and target range for correlation coefficient indicate that Cu/(Zn + Sn) ratio should be shifted to about 0.83 instead of previously defined 0.75 literature-reference value.

After the correct concentration range is settled and controlled, the mobility should be made as high as possible. The samples with close to carrier concentration range, i.e. *M3*, *L4* and *M2*, *L3*, and the highest mobility meet slightly tin-rich conditions for ratio Zn/Sn about 0.88 instead of the literature-reference 1.2 value (Fig. 8).

Finally, in Fig. 9, the mapping of all sample types versus the two composition ratios, together with literature-reference and stoichiometry

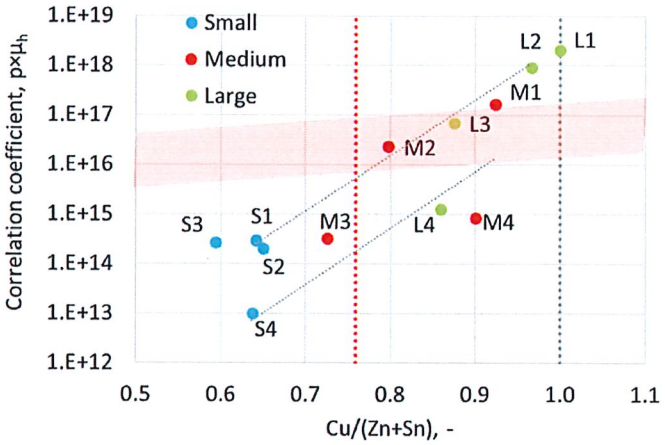

Fig. 7. Correlation coefficient versus Cu/(Zn + Sn) ratio with optimal range (in pink) from SCAPS predictions. Dashed vertical lines denote stoichiometric (black) and literature reference (red) ratios. Dotted oblique lines show the distribution of the samples along low S and high S iso-contents.

values, indicate that the best samples discussed above are shifted from the reference ratios towards 0.79 < Cu/(Zn + Sn) < 0.91 and 0.79 < Zn/Sn < 0.96.

4. Conclusions and perspectives

Three different groups of CZTS samples with four different RTP conditions have been studied in order to put in evidence the correlations between material composition and opto-electrical properties. SCAPS simulations have been performed to define the optimal range for opto-electrical parameters suiting our experiments: bandgap E_g ~1.5 eV, *hole concentration* p ~2 × 10^{15}–8 × 10^{15} cm^{-3} and hole mobility μ_h > 10 $cm^2V^{-1}s^{-1}$, to allow to break the 10% efficiency limit. The predicted single-junction cell efficiency for our best samples *M2*, *L3* is about 8%

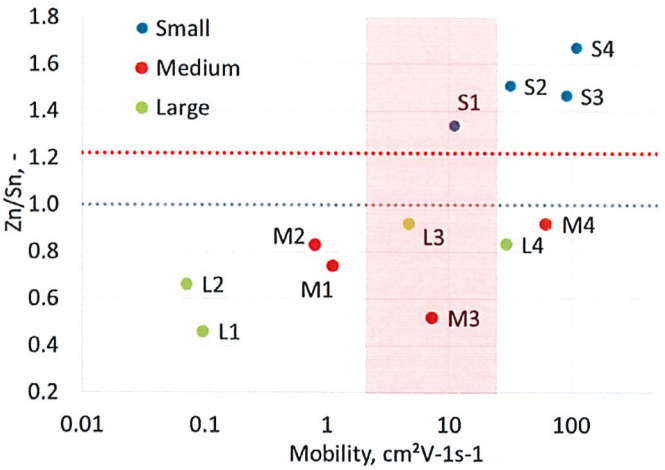

Fig. 8. Zn/Sn ratio versus mobility for all samples in this study with optimal range for mobility (shadowed pink zone). Dotted lines denote stoichiometric (black) and literature-reference (red) ratios.

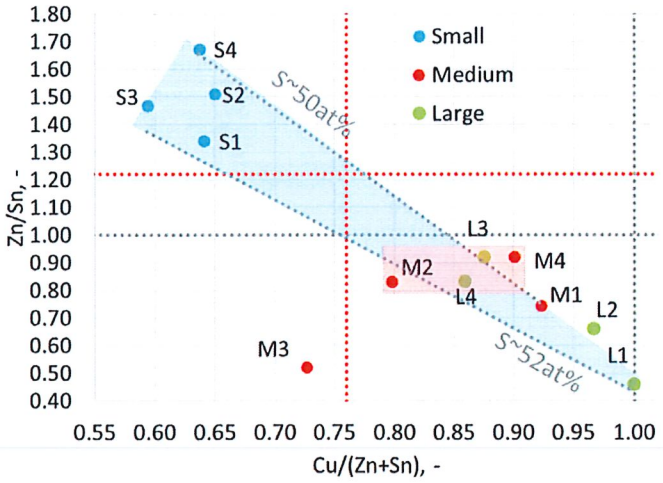

Fig. 9. Chart mapping of all sample types versus composition ratios together with literature-reference value (intersection of red dotted lines) and stoichiometry (intersection of grey dotted line) and our optimal zone (pink region).

according to their not yet fully-optimized optoelectronic properties. Other fabricated samples of S-type with low thickness and very low carrier concentration could be more suitable for tandem or single junction solar cell application.

Our results evidence the important correlation of carrier concentration and Hall mobility following a $\mu_h \sim p^{-0.4}$ trend and confirm the thermionic mechanism of conductivity [14]. Both opto-electrical parameters depend on compositional ratios in the final CZTS layers. For this study, the ***correlation coefficient*** $p \times \mu_h$ was introduced to put in evidence the optimal parameters. To reach the optimal values in optoelectrical properties, the composition reference ratios chosen from literature do not appear to be the best and should be shifted **towards a less Cu-poor and less Zn-rich region** with **Cu~22.3%, Zn~12.6%, Sn~14.3%, S~50.8%** atomic weights.

Future work should verify the new established tendencies for CZTS layer composition with metal back contact and the finished cell structure.

Author agreement statement

We the undersigned declare that this manuscript is original, has not been published before and is not currently being considered for publication elsewhere. We confirm that the manuscript has been read and approved by all named authors and that there are no other persons who satisfied the criteria for authorship but are not listed. We further confirm that the order of authors listed in the manuscript has been approved by all of us. We understand that the Corresponding Author is the sole contact for the Editorial process. She is responsible for communicating with the other authors about progress, submissions of revisions and final approval of proofs.

Declaration of competing interest

The authors declare that they have no known competing financial interests or personal relationships that could have appeared to influence the work reported in this paper.

Acknowledgments

The authors thank the Fund for Scientific Research (F.R.S.–FNRS) for support the FRFS-WISD project ID 29114491.

Appendix A. Supplementary data

Supplementary data to this article can be found online at https://doi.org/10.1016/j.mssp.2020.105367.

Appendix 1. SEM cross section views for some samples

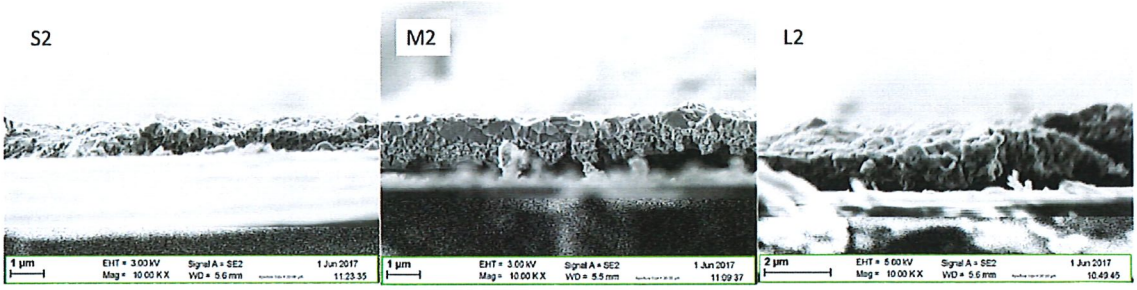

Appendix 2. Optical results and fitting curves

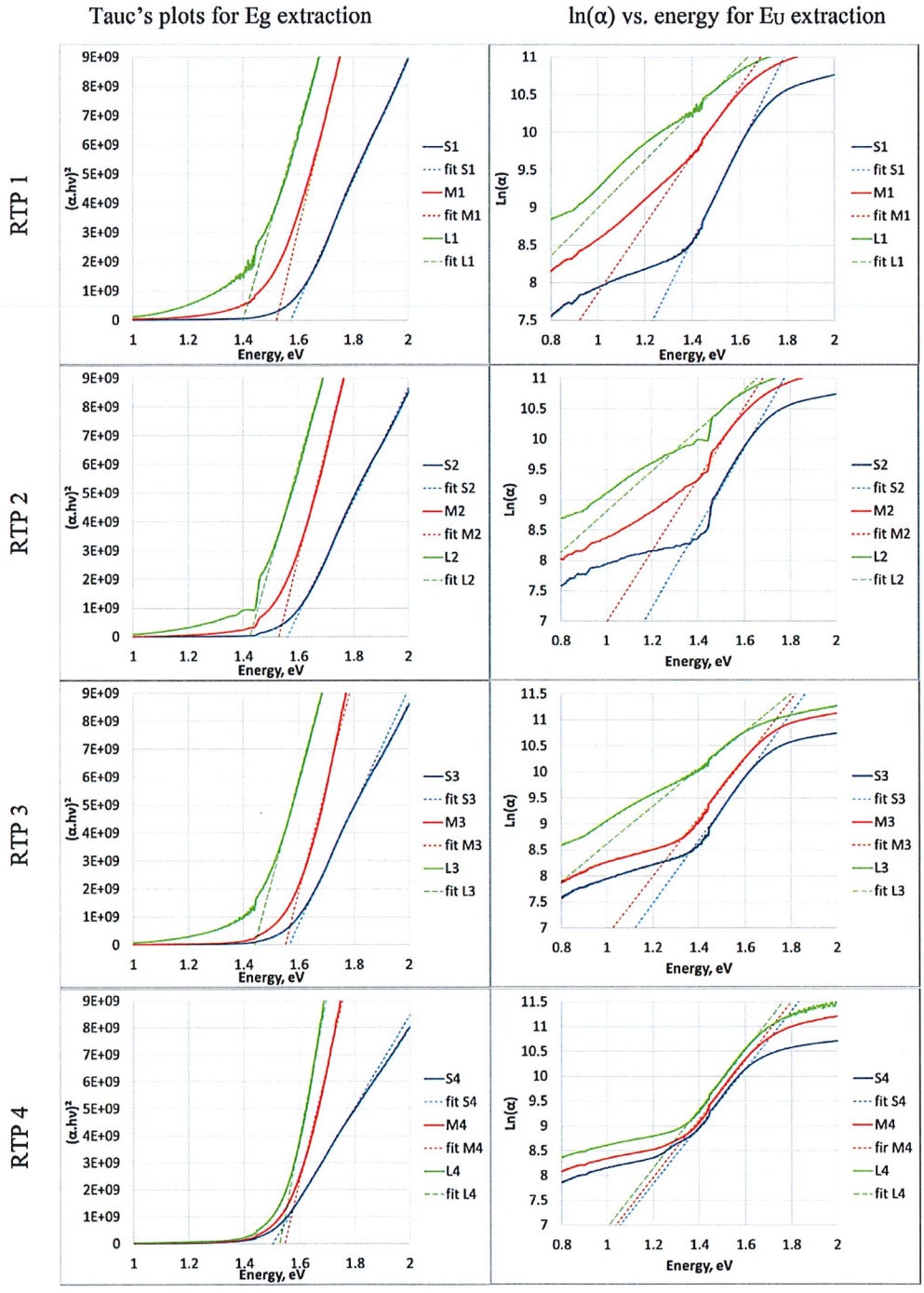

Appendix 3. Baseline parameters used for SCAPS modelling of CZTS solar cells

Parameter	CZTS	CdS	i-ZnO	ZnO:Al
E_g (eV)	1.2–1.6	2.4	3.3	3.3
χ (eV)	4.5	4.45	4.55	4.55
$\varepsilon/\varepsilon_0$	13.6	10	9	9
N_C (cm^{-3})	2.2×10^{18}	1.3×10^{18}	3.1×10^{18}	3×10^{18}
N_V (cm^{-3})	1.5×10^{19}	9.1×10^{18}	1.8×10^{19}	1.8×10^{19}
V_e (cm/s)	3.9×10^{7}	3.1×10^{7}	2.4×10^{7}	2.4×10^{7}
V_h (cm/s)	1.4×10^{7}	1.6×10^{7}	1.3×10^{7}	1.3×10^{7}
μ_e ($cm^2/V{\cdot}s$)	$4 \times \mu_h$	72	100	100
μ_h ($cm^2/V{\cdot}s$)	0.01–25	20	31	3
Doping (cm^{-3})	10^{11}-10^{19} (a)	1×10^{17} (d)	1×10^{17} (d)	5×10^{19} (d)
Bulk defect properties				
N (cm^{-2})	10^{14} (D)	5×10^{16} (A)	10^{16} (A)	10^{16} (A)
σ_e (cm^2)	10^{-15}	10^{-15}	10^{-15}	10^{-15}
σ_h (cm^2)	10^{-11}	5×10^{-13}	5×10^{-13}	5×10^{-13}

(a) and (d) denote shallow acceptor and donor defect while (A), (D) denote deep acceptor and donor defects.
Nomenclature: E_g: Band gap; $\varepsilon/\varepsilon_0$: Relative permittivity; χ: Affinity; μ_e, μ_h: Mobility of electrons and holes; N_C, N_V: Effective density of states in conduction and valence bands; σ_e, σ_h: Capture cross-section of electrons and holes.

References

[1] K. Ito, T. Nakazawa, Electrical and optical properties of stannite-type quaternary semiconductor thin films, Jpn. J. Appl. Phys. 27 (11) (1988) 2094–2097.
[2] T. Ratz, et al., Physical routes for the synthesis of kesterite, J. Phys. Energy 1 (2019), 042003, https://doi.org/10.1088/2515-7655/ab281c.
[3] J. He, et al., Cu2ZnSnS4 thin film solar cell utilizing rapid thermal process of precursors sputtered from a quaternary target/a promising application in industrial processes, J. Roy. Soc. Chem. Adv. 4 (2014) 4.080–43086.
[4] G. Ray, et al., On the origin of band-tails in kesterite, Sol. Energy Mater. Sol. Cells 179 (2018) 142–151.
[5] K. Kaur, et al., Strategic review of interface carrier recombination in earth abundant Cu-Zn-Sn-S-Se solar cells: current challenges and future prospects, J. Mater. Chem. A 5 (7) (2017) 3069–3090, https://doi.org/10.1039/c6ta10543b.
[6] A. Redinger, et al., Influence of S/Se ratio on series resistance and on dominant recombination pathway in Cu2ZnSn(SSe)4 thin film solar cells, Thin Solid Films 535 (2013) 291–295, https://doi.org/10.1016/j.tsf.2012.11.111.
[7] B. Vermang, et al., Rare surface optimization of CZTS solar cells by use of passivation layer with nanosized point openings, IEEE J. Photovolt. (2015) 2156–3381, https://doi.org/10.1109/JPHOTOV.2015.2496864.
[8] F. Liu, et al., Beyond 8% ultrathin kesterite Cu2ZnSnS4 solar cell by interface reaction route controlling g and self-organized nanopattern at the back contact, NPG Asia Mater. 9 (2017) e401, https://doi.org/10.1038/am.2017.103.
[9] S. Chen, et al., Intrinsic point defects and complexes in the quaternary kesterite semiconductor Cu2ZnSnS4, Phys. Rev. B 81 (2010) 245204.
[10] S. Delbos, Kesterite thin films for photovoltaics: a review, EPJ Photovolt. 3 (2012) 35004.
[11] C. Yan, et al., Cu2ZnSnS4 solar cells with over 10% power conversion efficiency enabled by heterojunction heat treatment, Nat. energy 3 (9) (2019) 764, https://doi.org/10.1038/s41560-018-0206-0.
[12] C. Malerba, et al., CTZS stoichiometry effects on the band gap energy, J. Alloys Compd. 582 (2014) 528–534.
[13] M.I. Amal, et al., The influence of the precursor compositional ratio on Cu_2ZnSnS_4 films prepared by using sulfurization of metallic precursor, J. Kor. Phys. Soc. 63–11 (2013) 2194–2198.
[14] O. Vigil-Galán, et al., Electrical properties of sprayed CZTS thin films and its relation with secondary phases formation and solar cell performance Solar Energy, Mater. Solar Cells 132 (2015) 557–562.
[15] H. Hazama, et al., Transport properties of the CZTS bulk system: effects of nonstoichiometry and defect formation, J. Alloys Compd. 657 (2016) 179–183.
[16] H. Hiroi, et al., High Voltage Cu2ZnSnS4 Submodules by Hybrid Buffer Layer, Conference Paper, 2013.
[17] K. Sun, et al., Beyond 9% efficient kesterite Cu2ZnSnS4 solar cell: fabricated by using Zn1-xCdxS buffer layer, Adv. Energy Mater. 6 (2016) 1600046, https://doi.org/10.1002/aenm.201600046(12).
[18] M. Zhukova, et al., Characterization and Simulation of CZTS Absorber Layers Fabricated by Sequential DC Magnetron Sputtering and Rapid Thermal Processing EUPVSEC Conference Proceeding, 2017.
[19] M. Patel, et al., Enhancement of output performance of Cu2ZnSnS4 thin film solar cells – a numerical simulation approach and comparison to experiments, Physica B 407 (2012) 4391–4397.
[20] M. Burgelman, et al., Advanced electrical simulation of thin film solar cells, Thin Solid Films 535 (2013) 296–301.
[21] Z. Jun, S. LeXi, Cu2ZnSnS4 thin films prepared by sulfurizing different multilayer metal precursors, Sci. China Technol. Sci. 52 (1) (2009) 269–272.
[22] P.A. Fernandes, et al., Cu2ZnSnS4 solar cells prepared with sulphurized dc-sputtered stacked metallic precursors, Thin Solid Films 519 (2010) 7382–7385.
[23] H. Yoo, J. Kim, Growth of CZTS thin films using the sacked metallic films, Thin Solid Films 518 (2010) 6567–6572.
[24] S.W. Shin, et al., Studies on Cu2ZnSnS4 (CZTS) absorber layer using different stacking orders on precursor thin films, Sol. Energy Mater. Sol. Cells 95 (2011) 3202–3206.
[25] S. Ranjbar, et al., Effect of Sn/Zn/Cu precursor stack thickness on two-step processed kesterite solar cells, Thin Solid Films (2016), https://doi.org/10.1016/j.tsf.2016.08.040.
[26] H. Wang, Progress in thin film solar cells based on Cu2ZnSnS4, Int. J. Photoenergy (2011), https://doi.org/10.1155/2011/801292.
[27] A. Fairbrother, et al., On the formation mechanism of Zn-rich Cu2ZnSnS4 films prepared by sulfurization of metallic stacks, Sol. Energy Mater. Sol. Cell. 112 (2013) 97–105.
[28] S. Zhou, et al., Growth of CZTS thin films by sulfurization of sputtered single-layered Cu-Zn-Sn metallic precursors from an alloy target, J. Mater. Sci. Mater. Electron. 24 (2013) 4958–4963, https://doi.org/10.1007/s10854-013-1507-5.
[29] C. Yan, et al., Kesterite Cu_2ZnSnS_4 solar cell from sputtered Zn/(Cu&Sn) metal stack precursor, J. Alloys Compd. 610 (2014) 486–491.
[30] S.M. Pawar, et al., Synthesis of CZTS absorber by rapid thermal processing sulfurization of stacked metallic precursor films for solar cell applications, Mater. Lett. 118 (2014) 76–79.
[31] R. Kotipalli, et al., Passivation effects of atomic-layer-deposited aluminium oxide, EPJ Photovolt. (2013) 445107, https://doi.org/10.1051/epjpv/2013023.
[32] P.E. Lobert, et al., Immobilization of DNA on CMOS compatible materials, Sensor. Actuator. B 92 (2003) 90–97.
[33] H. Katagiri, et al., The influence of the composition ration on CZTS-based thin film solar cells, Mater. Res. Soc. Symp. Proc. 1165 (2009).
[34] J. Just, et al., Secondary phases and their influence on the composition of the kesterite phase in CZTS and CZTSe thin films, Phys. Chem. Chem. Phys. (2016), https://doi.org/10.1039/C6CP00178E.
[35] J.J.S. Scragg, et al., Rapid annealing of reactivly sputtered precursors for Cu_2ZnSnS_4 solar cells, Progr. Photovolt. 22 (2014) 11–17.
[36] R. Liu, et al., Preparation of high-quality Cu2ZnSnS4 thin films for solar cells via the improvement of sulfur partial pressure using a static annealing sulfurization approach, Sol. Energy Mater. Sol. Cell. 157 (2016) 221–228.
[37] J.C. Gonzalez, et al., Influence of the sulfurization time on the morphological, chemical, structural and electrical properties of Cu2ZnSnS4 polycrystalline thin films, Sol. Energy Mater. Sol. Cell. 123 (2014) 58–64.
[38] H. Yoo, et al., Sulfurization temperature effects on the growth of Cu_2ZnSnS_4 thin film, Curr. Appl. Phys. 12 (2012) 1052–1057.
[39] Sung Chul Jung, Young-Kyu Han, Monoclinic sulfur cathode utilizing carbon for high-performance lithium-sulfur batteries, J. Power Sources 325 (2016) 495–500.
[40] C. Malebra, et al., Cation disorder in Cu_2ZnSnS_4 thin films: effect on solar cell performances, Thin Films Solar Cells (2017), https://doi.org/10.1002/solr.201700101.
[41] http://four-point-probes.com/ecopia-hms-3000-hall-measurement-system/.
[42] O. Gunawan, et al., A parallel dipole line system, Appl. Phys. Lett. 106 (2015), 062407.
[43] S.M. Pawar, et al., Growth of void free Cu_2ZnSnS_4 (CZTS) thin films by sulfurization of stacked metallic precursors films, Vacuum 104 (2014) 57–60.
[44] J.J. Scragg, et al., Chemical insights into the instability of Cu_2ZnSnS_4 films during annealing, Chem. Mater. 23 (2011) 4625–4633.
[45] P.-A. Cormier, et al., One-step synthesis of Cu2ZnSnS4 thin films by reactive magnetron co-sputtering, Acta Mater. 96 (2015) 80–88.
[46] M.Y. Valakh, et al., Raman scattering and disorder effect in Cu2ZnSnS4, Phys. Status Solidi RRL (2013) 1–4, https://doi.org/10.1002/pssr.201307073.
[47] J.J. Scragg, et al., A low-temperature order-disorder transition in Cu2ZnSnS4 thin films, Appl. Phys. Lett. 104 (2014), 041911.
[48] A.S. Hassanien, et al., Influence of composition on optical and dispersion parameters of thermally evaporated non-crystalline $Cd_{50}S_{50-x}Se_x$ thin films, J. Alloys Compd. 648 (2015) 280–290.

[49] M. Nishiwaki, et al., Tail state formation in solar cell materials: first principles analyses of zincblende, chalcopyrite, kesterite, 2018, 05106 arXiv: 1803.
[50] T. Kohl, et al., Fabrication of high band gap kesterite solar cell absorber materials for tandem applications, Thin Solid Films 660 (2018) 247–252.
[51] T. Gomken, et al., Band tailing and efficiency limitation in kesterite solar cells, Appl. Phys. Lett. 103 (2013) 1035061–1035065.
[52] C. Yan, et al., Beyond 11% efficient sulfide kesterite Cu2ZnxCd1-xSnS4 solar cell: effects of Cadmium alloying, ACS Energy Lett. 2 (2017) 930–936, https://doi.org/10.1021/qcsenergylett.7b00129.
[53] B. Ananthojo, et al., Cation/Anion substitution in CZTS for improved photovoltaic performance, Sci. Rep. 6 (2016), https://doi.org/10.1038/srep35369.